Alteration and Erosion of Rock Matrix Bordering a Carbonate-Rich Shale Fracture

Hang Deng[†‡], Marco Voltolini[†§], Sergi Molins[†], Carl Steefel[†], Donald DePaolo[†‡], Jonathan Ajo-Franklin[†], and Li Yang[†]

[†] Lawrence Berkeley National Laboratory, Berkeley, California 94720, United States

[‡] Earth and Planetary Science, University of California, Berkeley, Berkeley, California 94720, United States

Environ. Sci. Technol., **2017**, *51* (15), pp 8861–8868

DOI: 10.1021/acs.est.7b02063

Publication Date (Web): July 6, 2017

*Phone: 609-937-9927; e-mail: hangdeng@lbl.gov.

Abstract

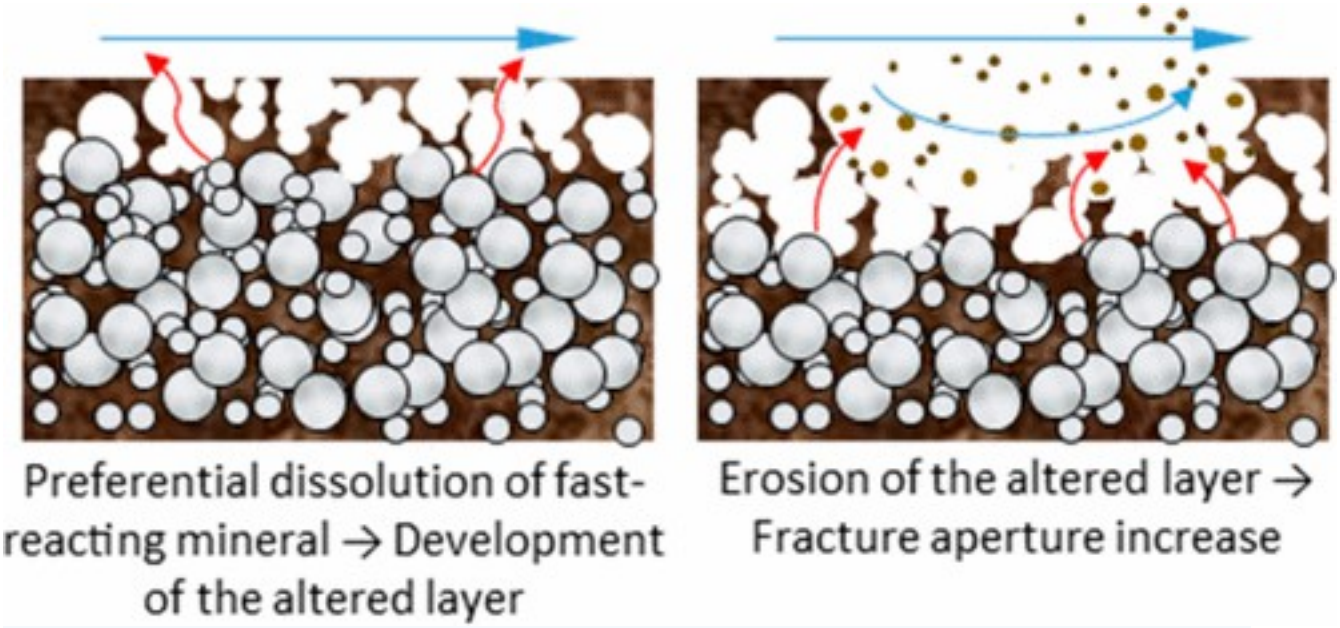

A novel reactive transport model has been developed to examine the processes that affect fracture evolution in a carbonate-rich shale. An in situ synchrotron X-ray microtomography experiment, flowing CO_2 saturated water through a single fracture mini-core of Niobrara Shale provided the experimental observations for the development and testing of the model. The phenomena observed included the development of a porous altered layer, flow channeling, and increasingly limited calcite dissolution. The experimental observations cannot be explained by models that consider only mineral dissolution and development of an altered layer. The difference between the fracture volume change recorded by the microtomography images and what would be expected from mineral dissolution alone suggest that there is erosion of the altered layer as it develops. The numerical

model includes this additional mechanism, with the erosion rate based on the thickness of the altered layer, and successfully captures the evolution of the geochemical reactions and morphology of the fracture. The findings imply that the abundance (with a threshold of approximately 35%) and reactivity of the rapidly reacting mineral control the development and erodibility of the altered layer on the fracture surfaces, and therefore fracture opening.

1 Introduction

Subsurface environments are a major source for energy production and storage, and an important site for waste disposal.(1) Fractures provide preferential flow conduits and can control the hydraulic properties of subsurface formations.(2) Fracture geometries and thus the hydraulic and geomechanical properties of subsurface formations are subject to changes caused by geochemical reactions.(3, 4) Therefore, understanding the dynamic evolution of fractures is critical for accurate assessment of the safety or profitability of different subsurface practices.

In the case of CO_2 injection for enhanced oil recovery or geological carbon storage reactive fluids are generated by CO_2 dissolution in reservoir brines.(5) As a result, the ambient chemical equilibrium is perturbed, and geochemical reactions between the reactive fluids and minerals take place, leading to porosity and permeability change of the reservoir formations and caprocks.(6, 7)For geological carbon storage systems, investigations of fracture evolution in carbonate-rich shales are of particular interest. Because shales are typical caprocks for containment of the injected CO_2,(8) and the dissolution of carbonates in shales as a result of advective flow of CO_2–acidified fluid introduced by fractures may raise concerns about caprock integrity and storage security.(9)

A number of experimental and numerical studies have been conducted to investigate fracture alteration driven by geochemical reactions. Studies have shown that dissolution of minerals can result in fracture opening, and fracture permeability increasing.(10-13) In systems with a single mineral, the dissolution of the mineral is limited to the inlet if the flow rate is slow compared to the reaction rate, and is uniformly distributed in the fracture when the flow rate is fast compared to the reaction rate.(12, 14, 15) In intermediate flow regimes, where the reaction rate and the flow rate are comparable, the dissolution is localized, accompanied by a dramatic increase in fracture permeability.(11, 12) Mineral precipitation, on the other hand, causes fracture sealing and results in decreases in the fracture hydraulic properties.(16) The extent and spatial pattern of precipitation depends on the saturation state of the fluid and the flow rate.(17)

In multimineral systems, mineral reactions have a more complex impact on the alteration of fracture geometries and the evolution of fracture hydraulic properties. It has been observed that if the reactive mineral grains are dispersed in rock matrix with less-/nonreactive minerals, a porous altered layer develops on the fracture surface.(10, 18-20) This altered layer may increase the roughness of the fracture surface and limit the increase of fracture permeability resulting from fracture opening. (21, 22) It can also create a barrier that limits the accessibility of the reactive mineral to the reactive fluid, thus reducing the overall dissolution rate of the fast-reacting mineral.(18, 23) Furthermore, it has been observed that this altered layer may detach from the fracture surface.(18, 19, 24) The released particles may be mobilized and transported downstream, where redeposition of the particles can cause clogging in the fractures and reduction of fracture permeability. However, to date, studies on how the development and erosion of the altered layer affects fracture evolution have been limited to qualitative observations.

In this study, we present a quantitative analysis of fracture geometry alteration in a carbonate-rich shale sample (Niobrara Shale) exposed to flowing CO_2-acidifed fluid. The experiment showed complex dynamics of fracture morphology and fluid chemistry because of the development and detachment of the altered layer on the fracture surfaces. We develop a reactive transport model that accounts for the evolution of both the effluent chemistry and the fracture geometry observed in the experiment. The manuscript concludes with a discussion of the environmental implications of our findings about the impacts of the development and erosion of an altered layer on fracture evolution.

2 Experimental Section

2.1 Experimental Setup and Materials

The sample used in the experiment was cylindrical (~9 mm in diameter and 25 mm long), and was cored from an outcrop near the CEMEX Lyons plant, between Lyons and Longmont, Colorado. The outcrop is a relatively carbonate-rich oil shale horizon within the Niobrara Formation (Denver Basin). The cylindrical axis of the core is roughly perpendicular to the bedding plane. Rietveld quantitative X-ray Powder Diffraction (XRPD) analysis on a fragment from the same block revealed that the mineralogical composition (weight %) of the rock is calcite (48.5%), Illite (17.5%), quartz (14.6%), dolomite (6.8%), smectite (6.6%), plagioclase (3.5%), pyrite (2.1%), and lesser amounts of other minerals.

The fracture flow experiment was performed using a custom-made triaxial flow cell optimized for synchrotron X-ray microcomputed tomography (SXRμCT) measurements. The experimental system

and procedures for in situ measurements are similar to those described in Ajo-Franklin et al. (2017). (20) The measurement was carried out at the hard X-ray imaging beamline 8.3.2. at the Advanced Light Source (ALS) located at Lawrence Berkeley National Laboratory.(25)

The sample was sawed along its cylinder axis to simulate a single planar fracture. The assembled sample was wrapped in PTFE tape and placed in PVDF heat-shrink tubing to isolate it from the confining fluid. The confining pressure in the system was controlled using a high-pressure syringe pump (ISCO 260D, Teledyne Technologies Inc.) set to ~117 bar. A second syringe pump was used to inject CO_2-rich water at a constant flow rate of 5 μL/min for the first ~40 h and at 10 μL/min for the rest of the experiment. The influent was prepared by equilibrating deionized water with CO_2 at ~34.5 bar overnight. The fluid was injected into the sample from the bottom side. Effluent samples were collected downstream of a 0.5 μm stainless steel filter every ~5 h, and later analyzed using inductively coupled plasma mass spectrometry (ICP-MS). The experiment was performed at room temperature, and during the ~104 h of flow, the pore pressure was maintained constant at ~96.5 bar using a back-pressure regulator.

Tomographic scans were acquired every ~20 h during flow to monitor the alteration of the fracture until 95.5 h. At each time step, given the limited vertical field of view, eight tiles were scanned along the flow direction to capture the entire sample. For each tile, 2049 projections were collected over a 180 deg rotation of the sample; the exposure time for a single projection was 150 ms. Filter-hardened (2 mm Al, 0.5 mm Cu) polychromatic X-rays were used to ensure a high photon flux at high energy, in order to achieve faster data collection (~2 h for each whole data set of eight tiles). The reconstruction of the tomographic volumes was conducted using a conventional filtered back-projection approach, with the Octopus software package. The resulting grayscale images have a voxel size of 6.7 μm. The eight tiles at each time step were stitched for subsequent image processing and analyses of the fracture geometry in imageJ.(26)

The resulting 3D volume data sets (e.g., Figure 1(a)) were cropped to isolate the fracture and then converted into binary volumes by applying a simple threshold. Voxels with grayscale values larger than the threshold are characterized as the solid phase, while the rest are classified as the fluid phase. The threshold was chosen based on careful visual inspection of the images. The same threshold value was applied to all six sets of volume images for consistent segmentation results.

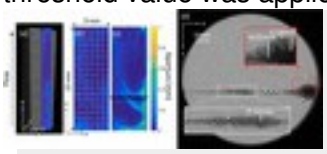

Figure 1. (a) An illustration of aperture map derivation from SXRμCT data, (b) aperture map representing the initial fracture geometry with an overlying mesh illustrating the 2D discretization (please note that this does

not show the actual mesh resolution), (c) aperture map of the post reaction fracture from image data collected at 95.5 h of the experiment, and (d) a slice of postreaction SXRμCT image perpendicular to the fracture plane located at ∼1 cm from the inlet (highlighted by the black line in (c)), illustrating localized fracture opening and the development of the altered layer. The white box in (d) highlights the region where altered layer develops but with no observable aperture change, and the red box highlights the altered layer in the flow channel.

2D maps of the fracture aperture, defined as the distance between two fracture surfaces, were then derived from the 3D binary volume images. The 3D Exact Euclidean Distance Transform (EEDT), which labels each voxel in phase #1 (fluid) with the distance to the closest voxel of phase #2 (solids), was first applied to the binary data sets. From the resulting 3D matrix, the maximum value of each column (along the z direction) that is perpendicular to the fracture plane (*x*–*y*) was calculated. This generates a 2D matrix, in which the values measure the distance between the fracture surface and the center of the void space. Multiplying the matrix by two produces the 2D aperture maps that can be readily visualized and compared quantitatively (e.g., Figure 1(b),(c)). The approach used for aperture calculation ensures that even though the altered layer has mixed mineral phases and void space, it is not counted as part of the fracture, with the exception of the spots where the altered layer only contains a small amount of remaining minerals and therefore is characterized as disconnected from the main rock volume.

2.2 Experimental Observations

ICP-MS analyses of the effluent samples showed variations in the concentrations of different cations over time (Figure 2). Calcium (Ca) has the highest concentration as a result of the rapid reaction rate of calcite. Before the flow rate change at 40 h, the Ca concentration displays no clear trend and shows an average of ∼25 mM. Afterward, it decreased gradually to ∼12 mM by 104 h. The trend indicates a considerable decrease in the overall calcite dissolution during the experiment. Previous studies have identified two mechanisms that can cause such substantial reduction: the diffusion limitation caused by an altered layer,(18, 23) and reduced effective fracture surface area for reaction because of flow channeling.(11) The SXRμCT images, discussed in detail below, indicate the presence of both mechanisms in our experiment.

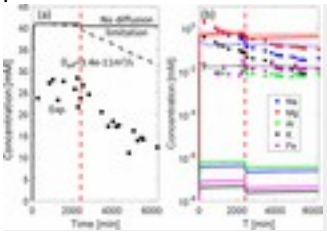

Figure 2. Effluent concentrations of (a) Ca, and (b) other major cations from the experimental measurements (dots), reactive transport simulation without the diffusion limitation of the altered layer (solid lines), the simulation with the diffusion limitation of the altered layer (dashed lines), and the simulation with diffusion limitation and consideration of the effects of ion exchange (dotted lines). The concentrations of cations other than Ca from the simulation with the diffusion limitation are similar to the results from the simulation without the diffusion limitation, and therefore do not show on (b). The simulation without the diffusion limitation of the altered layer reflect only the impacts of flow rate change (indicated by the vertical red dashed line). The simulation with the diffusion limitation of the altered layer uses an effective diffusion coefficient of 3.4×10^{-10} m^2/s.

The concentrations of other cations are mostly below 0.1 mM, with the exception of magnesium (Mg). These concentrations reflect the relatively rapid reaction rate of dolomite and lower reaction rates of the other minerals in the system. There is no clear trend in the temporal evolution of aluminum (Al) and iron (Fe), but the concentrations of sodium (Na), potassium (K) and Mg show a continuously decreasing trend over time. This trend is likely caused by ion exchange with the clay-bearing matrix as it is gradually exposed to Ca-rich fluid by the dissolution of calcite.

The SXRμCT images show fracture opening as a result of the exposure of the Niobrara fracture to CO_2-acidified fluid (Figure 1(c),(d)). The fracture volume estimated based on the fracture aperture maps increases from ~9.4 mm^3 to ~22 mm^3 by 95.5 h. The increase in fracture aperture is highly localized, and the spatial pattern correlates with the saw-cutting marks in the initial geometry.

The SXRμCT images (Figure 1(d)) and the high resolution tomography images (Supporting Information (SI) Figure S1) also show an altered layer on the fracture surface, which is created by the preferential dissolution of calcite and is primarily composed of the less reactive minerals (e.g., Illite, quartz) that remain in the rock matrix. Visual inspection indicates that the layer thickness is up to ~400 μm. The layer is located within the regions where fracture opening is observed. Because calcite has already been depleted in the rock matrix bordering the fracture (Figure 1(d)), fracture opening depends primarily on the removal of minerals other than calcite.

Mineral removal can be caused not only by dissolution but also by erosion of the altered layer, including disaggregation, particle detachment and removal by the fluid. In what follows, we compare changes in mineral volume from SXRμCT data and ICP-MS data to evaluate the relative importance of erosion as removal mechanism. The fact that the amount of mineral removal calculated from the SXRμCT data is considerably larger than the value estimated from effluent chemistry suggests that the opening of the Niobrara fracture is not solely the result of mineral dissolution.

If we were to assume that the effluent chemistry is only affected by mineral dissolution, the removal of mineral *m* can be calculated using eq 1,

$$\mathrm{dmol}_m = \frac{\int C_n \rho Q \, \mathrm{d}t}{\upsilon_{n,m}} \quad (1)$$

where C_n is the concentration of cation *n*, ρ and *Q* are the fluid density and volumetric flow rate, and $\upsilon_{n,m}$ is the stoichiometric coefficient of cation *n* in mineral *m*. Accordingly, the fracture volume change (d*V*) can be calculated from the dissolution of this mineral by eq 2,

$$\mathrm{d}V = \frac{\mathrm{dmol}_m \cdot \mathrm{MV}_m}{f_{0m}} \quad (2)$$

where MV_m and f_{0m} are the molar volume and volume fraction of mineral *m* in the intact rock matrix, respectively.

For example, given the mineralogical composition of the rock sample, Illite is likely the only source of K. Assuming a stoichiometric coefficient of 0.6 for K in Illite, the measured effluent K concentration indicates that the cumulative amount of Illite dissolution by the end of the experiment is approximately 0.004 mmol, and the corresponding fracture volume change would be 3.3 mm^3. In contrast, the fracture volume change by 95.5 h calculated from the SXRμCT data (12.6 mm^3) implies that 0.015 mmol of Illite was removed. This large discrepancy cannot be explained by uncertainties in image processing or mineralogy characterization. For example, the difference in the fracture volume change would indicate that the average aperture is overestimated by 37 μm in the SXRμCT data, or by more than five voxels averaged over the entire fracture. This seems to be highly unlikely. In addition, d*V* calculated from the effluent chemistry represents the upper limit of fracture volume change that can be caused by mineral dissolution. The cations (such as K) detected in the effluent chemistry may originate from three processes: (1) mineral dissolution in the sample, (2) dissolution of the fine particles that detach from the rock matrix and pass through the filter in the strong acid used for effluent sample preparation, and (3) ion exchange with Ca (which is not expected to cause mineral removal or fracture volume change). Since the signal of silica is nondetectable, it is unlikely that the fine particles released from erosion of the rock matrix passed through the filter and were included in the effluent analysis. In contrast, the contribution of ion exchange may be substantial, as will be discussed in the Simulation Section. This means that the above calculations overestimated the amount of Illite dissolution and the fracture volume change. Even with the overestimation, the resulting fracture volume increase is significantly lower than what was indicated by the image data, regardless of the uncertainties that may be introduced in image processing. Therefore, the removal of minerals that eventually caused the fracture opening in the Niobrara sample is not a result of mineral dissolution alone, but requires that erosion occurred as well.

Assuming symmetry, the average thickness of the altered layer on one side of the fracture surface can be estimated from the effluent Ca concentration and the fracture volume increase derived from

the SXRμCT images (dV_{CT}) using eq 3, where A is the area of the fracture plane. Based on the effluent analyses, the volume of the calcite dissolved is estimated to be ∼34 mm^3 and the average thickness of the altered layer is ∼150 μm on each side of the fracture surface. Please note that the thickness of the altered layer reported throughout the manuscript is always for one side of the fracture surface.

$$\bar{L} = \frac{\mathrm{dmol}_{cal} \cdot \mathrm{MV}_{cal} / \mathrm{f}_{0_{cal}} - \mathrm{dV}_{CT}}{2 \cdot A} \quad (3)$$

3 Simulation Section

3.1 Reactive Transport Model

The reactive transport model builds upon the 2.5D reactive transport model developed previously, (23) which was based on the software CrunchFlow.(27) The key features of the 2.5D model are summarized as follows. First, in the 2.5D model, the fracture is discretized in the two dimensions of the fracture plane (x–y) (Figure 1(b)). This approach can capture the variations in the fracture aperture and the resulting process of channelization as dissolution progresses. Second, within each grid cell, the model calculates the front position of each mineral according to its respective volume fraction in the grid and in the intact rock matrix. The fronts of all minerals are at the fracture surface initially, but diverge over time as a result of the differential reaction rates. The front of the mineral that retreats the slowest defines the new fracture surface, and the distance between the fronts of this mineral in the two fracture halves determines the flow aperture or fracture aperture. The distance between the fracture surface and the front of the mineral that reacts the fastest is the thickness of the altered layer, which with the effective diffusion coefficient of the altered layer is used to calculate the diffusion controlled reaction rate. An effective reaction rate is then calculated for the fast-reacting mineral based on both the diffusion controlled reaction rate and the surface reaction rate to account for any potential diffusion limitation caused by the altered layer. The caveat of the 2.5D model is that it assumes that the two fracture surfaces and their evolution are symmetric, which is an assumption that cannot be avoided without a full 3D treatment.

A new module has been added in the 2.5D model to simulate erosion of the altered layer in this study. As observed in the dissolution experiments of carbonate rocks by Garing et al. (2015),(28) in structured rock matrix, detachment and removal of mineral particles from the rock samples are caused by the preferential dissolution of the cementing material. Similarly, the altered layer is part of a structured rock matrix, and the mineral particles in the altered layer can only disaggregate and detach from the fracture surface freely when the cementing mineral (which is calcite in this case) is

dissolved. Therefore, the erosion of the altered layer depends on the extent of calcite reaction, which can be measured indirectly by the thickness of the altered layer (L (m)). Previous study(19)has also shown that the erosion of the altered layer is directly related to thickness of the altered layer. As such, we developed a phenomenological law (eq 4) for the erosion rate of the altered layer (E (m/s)), using L as the leading parameter. In eq 4, L_c is the critical thickness, below which no erosion takes place, η ($m^{1-\varepsilon}s^{-1}$) is the multiplying factor, and ε is the exponent.

$$E = \begin{cases} \eta(L - L_c)^{\varepsilon} & L > L_c \\ 0 & L \le L_c \end{cases} \quad (4)$$

We note that the formulation is similar to that typically used to describe erosion of uncemented sediments,(29) but the underlying mechanisms are different. In the erosion of the altered layer, the degree of weathering of the cementing material in the shale is the limiting factor, as opposed to fluid flow in the erosion process of sediments (see also the SI).

In grid cells where the erosion rate is nonzero, the aperture (b) is updated according to eq 5,

$$b_{i,j}^{t} = b_{i,j}^{t-1} + 2 \cdot E \cdot \mathrm{d}t \quad (5)$$

where the factor of 2 is used to account for erosion on both sides of the fracture surface with the assumption that the altered layer development is symmetric on the two fracture halves. The volume fractions of minerals remaining in the altered layer are updated using eq 6,

$$f_{i,j,m}^{t} = f_{i,j,m}^{t-1} - 2 \cdot E \cdot \mathrm{d}t \cdot \mathrm{d}x \cdot \mathrm{d}y \cdot f_{0_{i,j,m}} \quad (6)$$

where $f_{i,j,m}{}^{t}$ is the volume fraction of the mineral in the cell and $f_0 i,j,m$ is the volume percent of that mineral measured for the intact rock matrix.

A 2D mesh with quadrilateral cells in the fracture plane is used in the simulation, and is based on the initial aperture map derived from the SXRμCT data (Figure 1(b)). The original aperture map has a resolution of 6.7 μm following the SXRμCT image, and is downsampled by a factor of 10 so that the 2D computational mesh has a grid size ($\Delta x = \Delta y$) of 67 μm. The aperture of each grid cell is the arithmetic mean of the 10 × 10 patch. The reactive surface area is the geometric surface area within each grid, that is, $2\Delta x\Delta y$, and is divided among different minerals according to their respective volume fractions. In the simulations, influent chemistry and flow rate are those corresponding to the experiment, and the mineral composition in each grid cell is the same following the XRPD measurement. All mineral reactions are treated kinetically using transition state theory rate laws and kinetic data from the literature.(23, 30, 31) The thermodynamic and kinetic data of all mineral reactions are summarized in the SI.

Two sets of simulations are presented in the following subsections. Subsection 3.2 reports the results of simulations that consider factors such as flow rate change, mineral dissolution, and the diffusion limitation associated with the development of an altered layer. These simulations provide a

basis for comparison to the simulation presented in subsection 3.3, which adds the erosion of the altered layer.

3.2 Simulation Results without Erosion of the Altered Layer

3.2.1 Ca Concentration

As shown in Figure 2(a), the decrease in the effluent Ca concentration cannot be explained by the increase of flow rate, and is partly attributed to the development of the altered layer. As reported in our previous study,(23) the development of the altered layer imposes a diffusion limitation on the dissolution of the fast-reacting mineral, which leads to a reduction in effluent Ca. However, the diffusion limitation cannot fully account for the reduction in the effluent Ca concentration in this study. The effective diffusion coefficient used to calculate the diffusion limitation of the altered layer is 3.4×10^{-10} m^2/s, which is estimated based on a porosity of 58% using Archie's law with a constant of 1 and a cementation factor of 2 for the Niobrara Shale.(32) Analyses of the altered layer using the high resolution tomography images (see SI) showed that the altered layer porosity ranges from 49% to 68%, with an average of 58%. The images also showed connected void space (i.e., pathways) that tends to reduce tortuosity and therefore result in a higher effective diffusion coefficient for a given porosity. Even if a lower porosity in the reasonable range is assumed, the corresponding effective diffusion coefficient is not low enough, that is, the diffusion limitation on calcite dissolution is not strong enough to match the experimental observations (see SI).

In the simulation, the absolute values of effluent Ca concentration are overestimated. For example, the effluent Ca concentration before the flow rate change at 40 h produced by the model is 41 mM, substantially higher than the observed value of ~25 mM (Figure 2(a)). This means that effluent concentrations are overestimated by a factor of 1.5, which may be caused by uncertainties introduced in effluent sample collection and processing, in kinetic parameters,(33) and/or in reactive surface area.(34) However, adjusting the reaction rate of calcite does not explain the observed discrepancy in the *temporal evolution* of Ca concentration between the model and the experiment (see SI).

3.2.2 Concentrations of Cations Other Than Ca

As shown in Figure 2(b), the simulated concentration of Mg is on the order of 0.1 mM, within the range of the experimental observations. The simulated concentrations of all other cations from dissolution of minerals such as Illite and plagioclase are more than 5 orders of magnitude lower than the experimental measurements. Such dramatic discrepancies cannot be entirely attributed to uncertainties in the kinetic coefficients. For example, the reaction kinetic data for smectite compiled in Marty et al. (2015)(31) showed variations within 1 order of magnitude for a given pH and temperature.

The relatively high concentrations of Na and K measured from the effluent samples are likely the result of ion exchange, because the Ca-rich fluid created by calcite dissolution can displace other cations from the exchange sites in the clay minerals. It is also supported by the fact that the cumulative amount of these cations measured in the effluent chemistry (e.g., Na: 0.013 mmol) is within the range of the equivalents (0.005–0.05 mequiv) that would be released into the fluid as a result of ion exchange within the altered layer (with an average depth of 150 um) for typical Cation Exchange Capacity (CEC) values of 10–100 mequiv/100 g clay minerals (see SI). Figure 2(b) also plots the simulated cation concentrations from an approximate model that treats ion exchange as a dissolving salt phase (see SI for further discussion). The concentrations are within the range of the experimental observations, but show flatter decreasing trends. This is because the processes that affect the exchange reactions, such as the diffusion of Ca into the intact rock matrix and the resulting ion exchange (see SI), cannot be captured unless a full treatment of the dimension that is perpendicular to the fracture plane is implemented. Given the complications with considering ion exchange as a subgrid effect in the model, cations other than Ca are not discussed further in the manuscript.

3.2.3**Fracture Morphology Alteration**

Since mineral dissolution is the only mechanism for mineral removal in this simulation, the slow dissolution rates of the minerals that remain in the altered layer do not lead to an observable change in the fracture apertures. In contrast, the dissolution of calcite leads to a rapid retreat of the calcite front, resulting in substantial localized development of the altered layer (Figure 3(a)). The thickness of the altered layer is up to 0.642 mm, with an average value of 0.234 mm. The spatial pattern of the altered layer, which illustrates the degree of weathering on the fracture surface, shows a close match with the aperture change observed in the experiment. This observation further supports the approach adopted in the following subsection in which the erosion rate is formulated using the thickness of the altered layer as the leading parameter.

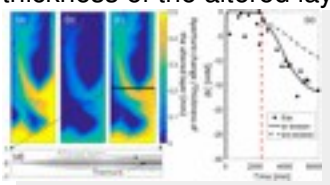

Figure 3. (a) Thickness of the altered layer on a single side of the fracture surface at 95.5 h from the simulation with diffusion limitation of the altered layer only, (b) fracture aperture change at 95.5 h from the simulation with the erosion of the altered layer and the corresponding (c) thickness of the altered layer, (d) a cross-section (at the black line in (c)) illustrating the simulated altered layer development bordering the fracture, and (e) the decrease in effluent Ca concentration observed in the experiment and simulated by the

simulations with (solid line) and without (dashed line) the erosion of the altered layer. The effective diffusion coefficient used for the simulations is 3.4×10^{-10} m^2/s.

The simulation results collectively confirm that although the development of the altered layer contributes to the decrease of calcite dissolution, this cannot fully explain by itself the evolution of the fracture morphology observed in the experiment and the resulting impact on overall calcite dissolution. Therefore, the contribution of one or more additional mechanisms is required.

3.3 Simulation Results with Erosion of the Altered Layer

When the erosion of the altered layer is considered, the simulation results can successfully capture the major features of the evolution of the Niobrara fracture observed in the experiment.

Following the removal of the altered layer, fracture apertures increase, resulting in a fracture volume increase of ~14 mm^3 by 95.5 h, which is comparable to the fracture volume change derived from the SXRμCT data. Although there is an 11% difference, it is comparable to the uncertainty in the volume estimation that can be introduced during image processing, since the difference translates to an overestimation of 5.9 μm in the average aperture, which is smaller than the size of one voxel. Since fracture aperture change is highly localized, the difference in fracture aperture between the simulation and the experiment vary spatially. For example, the aperture in the penetrating channel is different by up to 30%.

Overall, the simulated aperture change (Figure 3(b)), shows a spatial pattern that is similar to that recorded in the aperture maps derived from the SXRμCT data (Figure 1(c)). As indicated by the formulation of the erosion rate, the aperture increase resulting from the erosion of the altered layer depends primarily on the thickness of the altered layer. In our model, the aperture increase is a result of the localized development of the altered layer and its subsequent erosion. The initial flow variation triggers the localized development of the altered layer along the preferential flow path. When the altered layer reaches the critical thickness, the erosion process starts and the fracture aperture increases locally. The resulting flow channeling supplies additional reactive fluid in the enlarged region of the fracture, further promoting local calcite dissolution and altered layer development and erosion.

Flow channeling provides another mechanism that reduces overall calcite dissolution, in addition to the diffusion limitation of the altered layer. Because the reactive fluid is increasingly directed into the flow channel, and the interaction between the reactive fluid and fracture surfaces outside of the channel becomes limited. As a result, the effluent Ca concentration decreases further (Figure 3(e)). Because of the erosion and flow channeling, the simulated altered layer (Figure 3(c)) is slightly more localized and thinner in comparison with the simulation results in subsection 3.2 (Figure 3(a)). It has

an average thickness of 0.193 mm, with the maximum value being 0.529 mm. These values are higher than the estimates determined from the images and the effluent chemistry. This is because in the simulations the calcite reaction rate is overestimated, as discussed in the previous section.

To summarize, incorporating the erosion of the altered layer completes the positive feedback circle: flow-reaction - development of the altered layer - erosion of the altered layer–flow. This positive feedback explains why the spatial pattern of the aperture increase shows features of the initial fracture geometry and why overall calcite dissolution simulated by the model with the erosion of the altered layer is further reduced from what is calculated from the simulation that considers only the development of the altered layer in subsection 3.2 (Figure 3(e)).

4 Discussion

The erosion rate of the altered layer is determined by three parameters–the multiplying factor (η), the critical thickness of the altered layer (L_c), and the exponent (ε). In general, a larger η, or a smaller L_c, or a smaller ε (for thickness in meters and therefore smaller than unity) results in a higher erosion rate. The higher erosion rate leads to larger fracture opening and thus stronger flow channeling, and a thinner altered layer (see SI). As a result, the relative contribution to calcite dissolution reduction from flow channeling increases, while that of the altered layer diffusion limitation decreases. It is expected that the three parameters and thus the erosion rate are dependent on the composition of the altered layer, and therefore the chemical and physical properties of the original rock matrix. The three coefficients can be constrained using the five experimental observations in our study - the spatial pattern of aperture change, the extent of aperture change, the spatial pattern of the altered layer, the thickness of the altered layer, and the temporal evolution of the major cation.

In this simulation, L_c was constrained based on the SXRμCT images. The postreaction images showed regions where an altered layer develops while the fracture aperture does not change significantly (Figure 1(d)). The maximum thickness of the altered layer in these regions is determined to be ~0.14 mm. Based on this observation, the threshold value was chosen to be 0.15 mm. The other two parameters, ε and η, were varied such that the simulated effluent Ca concentration and aperture change both agree with the experimental observations (see SI for sensitivity analyses). The resulting exponent is 0.5, and η is 1 $m^{0.5}/s$. Even though it is difficult to define an optimal match, partly due to the uncertainties associated with the experimental characterization, reasonable agreement can be achieved and the results provide valuable insights regarding the erosion of the altered layer and its impacts on fracture evolution.

One other consideration that is important for assessing the role of altered layer erosion is the abundance of the fast-reacting mineral(s) as well as potentially the microgeometry and how important the fast-reacting phase is as a cement. In a previous experiment, where fast-reacting calcite constituted about 10% of the rock volume (the remainder being mostly dolomite), there was no evidence of erosion.(23) This suggests that this volume fraction is too low to cause the remaining undissolved matrix material to disaggregate. In the current study, the fast-reacting phase, that is, the microcrystalline calcite that cements the less reactive phases, is uniformly distributed in the matrix and constitutes 48% of the Niobrara Shale sample by volume. This is clearly sufficient to cause matrix disaggregation and erosion. These values are consistent with the range in abundance of fast-reacting mineral(s) reported in previous experimental studies that also observed particle mobilization from fracture surfaces that were exposed to reactive fluid flow, e.g. 45% of calcite in the carbonate caprock used in Ellis et al. (2013) and 65% of calcite in the argillaceous limestone studied by Noiriel et al. (2007).(18) These values are also consistent with observations of natural shales that show that a clay fraction of greater than about 35% results in the nonclay grains being supported by clay matrix.(35) The Niobrara sample has a clay fraction of <35% and relies on other minerals (calcite in particular) to provide the load-bearing framework,(35) and therefore removal of the framework by dissolution leaves the clay particles susceptible to disaggregation. 35% may also be a reasonable threshold for the fast-reacting mineral(s), above which erosion of the altered layer takes place. When the fast-reacting mineral(s) exceeds this threshold, as in the case of the clay matrix, it constitutes a continuous framework that provides the structural support for the matrix. The removal via dissolution of the fast-reacting mineral is most likely to result in disaggregation of the remaining minerals. As such, it is to be expected that 48% carbonate removed by dissolution should lead to disaggregation (and erosion) of the remaining matrix, while 10% carbonate removed by dissolution would not.

In the experiment, no systematic clogging was observed, and the SXRμCT images show consistent fracture opening. The lack of clogging is likely a result of the fine particle size of the remaining minerals that make up the altered layer (below the resolution of the SEM images and high resolution tomography), which based on the Stokes law correlates to extremely low settling velocity.(29) Furthermore, the erosion of the altered layer is focused in the main channel, where the apertures are large enough to allow the flow-through of a significant load of particles. However, clogging in regions with extremely fine apertures cannot be ruled out, as the noise and resolution make it difficult to identify or differentiate the fine particles during image processing. Garing et al. (2015)(28) provided a thorough discussion of particle mobilization and deposition in carbonate rocks, but further mechanistic investigations of clogging are needed, especially in fractures.

The lack of fracture closing under confining pressure observed in the Niobrara experiment indicates that localized erosion of the altered layer may allow persistent fracture opening. The limited development and thus erosion of the altered layer in the nonchannelized region (Figure 3(c)) means that the contact points in this region are not removed or weathered, and therefore are likely to prevent the fracture from closing under the confining stress.

In summary, our experiment and simulations show that the preferential dissolution of reactive minerals can trigger complex fracture alteration in multimineral systems, indicating that the evolution of a fracture driven by dissolution reactions cannot always be estimated simply based on the extent of mineral dissolution. The development of an altered layer at the fracture wall can limit subsequent reaction and thus prevent the change of fracture permeability if the porous altered layer remains intact. We argue that the development of the altered layer may also lead to eventual fracture opening not only because of the dissolution of the minerals composing the altered layer,(23) but also because of the erosion of the altered layer. This case should apply when the rapidly dissolving minerals is abundant (e.g., with volume fraction >35%). Our simulations illustrate that the erodibility of the altered layer depends largely on the thickness of the altered layer. As a result, the dissolution rate of the fast-reacting mineral (calcite here), which controls the development of the altered layer, will also determine the fracture aperture change.

Supporting Information

The Supporting Information is available free of charge on the ACS Publications website at DOI: 10.1021/acs.est.7b02063.

- Details of the reactive transport model. Image processing for altered layer porosity characterization. Ion exchange and cation release from the rock matrix into the fracture flow. Erosion of the altered layer in comparison with the erosion of sediments. Sensitivity analysis of the evolution of calcite dissolution to diffusion coefficients and calcite surface area. Sensitivity analysis of the erosion rate of the altered layer to different parameters (PDF)

- **PDF**
  - es7b02063_si_001.pdf (860.52 kB)

Supplemental Information: Alteration and erosion of rock matrix bordering a carbonate-rich shale fracture

Hang Deng[1,*], Marco Voltolini[1,†], Sergi Molins[1], Carl Steefel[1], Donald DePaolo[1, 2], Jonathan Ajo-Franklin[1], Li Yang[1]

1. Lawrence Berkeley National Laboratory, Berkeley, CA, 94720
2. Earth and Planetary Science, University of California, Berkeley, Berkeley, CA, 94720

*email: hangdeng@lbl.gov, cell: 609-937-9927

† Co-lead author

Table of Contents

List of Figures

List of Tables

The authors declare no competing financial interest.

§Author Status
Co-lead authors.

Acknowledgment

This work was supported as part of the Center for Nanoscale Controls on Geologic CO_2 (NCGC), an Energy Frontier Research Center funded by the U.S. Department of Energy, Office of Science, Basic Energy Sciences under Award # DE-AC02-05CH11231. Tomography experiments discussed were performed with the assistance of Dula Parkinson and Alastair MacDowell at the Advanced Light Source, Beamline 8.3.2, supported by the Office of Basic Energy Sciences, U.S. DOE (contract DE-AC02-05CH11231). The sample used for the experiment was provided by Timothy Kneafsey at Lawrence Berkeley National Laboratory.

Reference QuickView

References

This article references 35 other publications.

1. 1.

Pyrak-Nolte, L. J.; DePaolo, D. J.; Pietraß, T. *Controlling Subsurface Fractures and Fluid Flow: A Basic Research Agenda.*; USDOE Office of Science (SC): United States, **2015**.

[Crossref]

2. 2.

DePaolo, D. J.; Orr, F. M., Jr. Geoscience research for our energy future *Phys. Today* **2008**, 61 (8) 46– 51DOI: 10.1063/1.2970212

[Crossref]

3. 3.

Berkowitz, B. Characterizing flow and transport in fractured geological media: A review *Adv. Water Resour.***2002**, 25 (8–12) 861– 884 DOI: 10.1016/S0309-1708(02)00042-8

[Crossref], [CAS]

4. 4.

Carroll, S.; Carey, J. W.; Dzombak, D.; Huerta, N. J.; Li, L.; Richard, T.; Um, W.; Walsh, S. D. C.;Zhang, L. W. Review: Role of chemistry, mechanics, and transport on well integrity in CO2 storage environments *Int. J. Greenhouse Gas Control* **2016**, 49, 149– 160 DOI: 10.1016/j.ijggc.2016.01.010

[Crossref], [CAS]

5. 5.

Fitts, J. P.; Peters, C. A., Caprock Fracture Dissolution and CO2 Leakage. In *Geochemistry of Geologic Co2 Sequestration*; DePaolo, D. J.; Cole, D. R.; Navrotsky, A.; Bourg, I. C., Eds.; Mineralogical Soc Amer:Chantilly, **2013**; Vol. 77, pp 459– 479.

[Crossref]

6. 6.

Kampman, N.; Bickle, M.; Wigley, M.; Dubacq, B. Fluid flow and CO2-fluid-mineral interactions during CO2-storage in sedimentary basins *Chem. Geol.* **2014**, 369, 22– 50 DOI: 10.1016/j.chemgeo.2013.11.012

[Crossref], [CAS]

7. 7.

Zhang, L. W.; Soong, Y.; Dilmore, R.; Lopano, C. Numerical simulation of porosity and permeability evolution of Mount Simon sandstone under geological carbon sequestration conditions *Chem. Geol.* **2015**, 403, 1– 12DOI: 10.1016/j.chemgeo.2015.03.014

[Crossref], [CAS]

8. 8.

Celia, M. A.; Bachu, S.; Nordbotten, J. M.; Bandilla, K. W. Status of CO2 storage in deep saline aquifers with emphasis on modeling approaches and practical simulations *Water Resour. Res.* **2015**, 51 (9) 6846– 6892DOI: 10.1002/2015WR017609

[Crossref], [CAS]

9. 9.

Gherardi, F.; Xu, T. F.; Pruess, K. Numerical modeling of self-limiting and self-enhancing caprock alteration induced by CO2 storage in a depleted gas reservoir *Chem. Geol.* **2007**, 244 (1–2) 103– 129 DOI: 10.1016/j.chemgeo.2007.06.009

[Crossref], [CAS]

10. 10.

Ellis, B. R.; Peters, C.
A.; Fitts, J.; Bromhal, G.; McIntyre, D.; Warzinski, R.; Rosenbaum, E. Deterioration of a fractured carbonate caprock exposed to CO2-acidified brine flow *Greenhouse Gases: Sci. Technol.* **2011**,1 (3) 248– 260 DOI: 10.1002/ghg.25

[Crossref], [CAS]

11. 11.

Deng, H.; Fitts, J. P.; Crandall, D.; McIntyre, D.; Peters, C. A. Alterations of Fractures in Carbonate Rocks by CO2-Acidified Brines *Environ. Sci. Technol.* **2015**, 49 (16) 10226– 10234 DOI: 10.1021/acs.est.5b01980

[ACS Full Text], [CAS]

12. 12.

Elkhoury, J. E.; Ameli, P.; Detwiler, R. L. Dissolution and deformation in fractured carbonates caused by flow of CO2-rich brine under reservoir conditions *Int. J. Greenhouse Gas Control* **2013**, 16 (Supplement 1, (0))S203– S215 DOI: 10.1016/j.ijggc.2013.02.023

[Crossref], [CAS]

13. 13.

Noiriel, C.; Gouze, P.; Made, B. 3D analysis of geometry and flow changes in a limestone fracture during dissolution *J. Hydrol.* **2013**, 486, 211– 223 DOI: 10.1016/j.jhydrol.2013.01.035

[Crossref], [CAS]

14. 14.

Detwiler, R.; Glass, R.; Bourcier, W. Experimental observations of fracture dissolution: The role of Peclet number on evolving aperture variability *Geophys. Res. Lett.* **2003**, 30 (12) 1648– 1651 DOI: 10.1029/2003GL017396

[Crossref]

15. 15.

Szymczak, P.; Ladd, A. J. C. Wormhole formation in dissolving fractures *J. Geophys. Res.* **2009**, 114,B06203 DOI: 10.1029/2008JB006122

[Crossref]

16. 16.

Jones, T. A.; Detwiler, R. L. Fracture sealing by mineral precipitation: The role of small-scale mineral heterogeneity *Geophys. Res. Lett.* **2016**, 43 (14) 7564– 7571 DOI: 10.1002/2016GL069598

[Crossref], [CAS]

17. 17.

Singurindy, O.; Berkowitz, B. The role of fractures on coupled dissolution and precipitation patterns in carbonate rocks *Adv. Water Resour.* **2005**, 28 (5) 507– 521 DOI: 10.1016/j.advwatres.2005.01.002

[Crossref], [CAS]

18. 18.

Noiriel, C.; Made, B.; Gouze, P. Impact of coating development on the hydraulic and transport properties in argillaceous limestone fracture *Water Resour. Res.* **2007**, 43 (9) W09406 DOI: 10.1029/2006WR005379

[Crossref], [CAS]

19. 19.

Andreani, M.; Gouze, P.; Luquot, L.; Jouanna, P. Changes in seal capacity of fractured claystone caprocks induced by dissolved and gaseous CO2 seepage *Geophys. Res. Lett.* **2008**, 35 (14) L14404 DOI: 10.1029/2008GL034467

[Crossref], [CAS]

20. 20.

Ajo-Franklin, J. V.; Marco; Molins; Sergi; Yang, Li, Coupled Processes in a Fractured Reactive System: A Dolomite Dissolution Study with Relevance to GCS Caprock Integrity. In *Caprock Integrity in Geological Storage: Hydrogeochemical and Hydrogeomechanical Processes and their Impact on Storage Security*;Wiley Publishing: **2017**; Vol. in press.

21. 21.

Deng, H.; Ellis, B. R.; Peters, C. A.; Fitts, J. P.; Crandall, D.; Bromhal, G. S. Modifications of Carbonate Fracture Hydrodynamic Properties by CO2-Acidified Brine Flow *Energy Fuels* **2013**, 27 (8) 4221– 4231 DOI: 10.1021/ef302041s

[ACS Full Text], [CAS]

22. 22.

Gouze, P.; Noiriel, C.; Bruderer, C.; Loggia, D.; Leprovost, R., X-ray tomography characterization of fracture surfaces during dissolution. *Geophys. Res. Lett.* **2003**, 30, (5). n/a DOI: 10.1029/2002GL016755

[Crossref]

23. 23.

Deng, H.; Molins, S.; Steefel, C.; DePaolo, D.; Voltolini, M.; Yang, L.; Ajo-Franklin, J. A 2.5D Reactive Transport Model for Fracture Alteration Simulation *Environ. Sci. Technol.* **2016**, 50 (14) 7564– 7571 DOI: 10.1021/acs.est.6b02184

[ACS Full Text], [CAS]

24. 24.

Ellis, B. R.; Fitts, J. P.; Bromhal, G. S.; McIntyre, D. L.; Tappero, R.; Peters, C. A. Dissolution-Driven Permeability Reduction of a Fractured Carbonate Caprock *Environ. Eng. Sci.* **2013**, 30 (4) 187– 193 DOI: 10.1089/ees.2012.0337

[Crossref], [PubMed], [CAS]

25. 25.

MacDowell, A. A.; Parkinson, D. Y.; Haboub, A.; Schaible, E.; Nasiatka, J. R.; Yee, C. A.; Jameson, J. R.;Ajo-Franklin, J. B.; Brodersen, C. R.; McElrone, A. J. *Proc. SPIE* **2012**, 2012, 850618– 850618–14 DOI: 10.1117/12.930243

[Crossref]

26. 26.

Abramoff, M. D.; Magelhaes, P. J.; Ram, S. J. Image Processing with ImageJ *Biophotonics International***2004**, 11 (7) 36– 42

27. 27.

Steefel, C. I.; Appelo, C. A.
J.; Arora, B.; Jacques, D.; Kalbacher, T.; Kolditz, O.; Lagneau, V.; Lichtner, P. C.;Mayer, K. U.; Meeussen, J. C.
L.; Molins, S.; Moulton, D.; Shao, H.; Simunek, J.; Spycher, N.;Yabusaki, S. B.; Yeh, G. T. Reactive transport codes for subsurface environmental simulation *Computational Geosciences* **2015**, 19 (3) 445– 478 DOI: 10.1007/s10596-014-9443-x

[Crossref]

28. 28.

Garing, C.; Gouze, P.; Kassab, M.; Riva, M.; Guadagnini, A. Anti-correlated Porosity-Permeability Changes During the Dissolution of Carbonate Rocks: Experimental Evidences and Modeling *Transp. Porous Media***2015**, 107 (2) 595– 621 DOI: 10.1007/s11242-015-0456-2

[Crossref], [CAS]

29. 29.

Leeder, M. R. *Sedimentology and Sedimentary Basins: From Turbulence to Tectonics*; Wiley-Blackwell:Chichester, West Sussex, UK, **2011**.

30. 30.

Palandri, J. L. K.; Yousif, K. *A Compilation of Rate Parameters of Water-Mineral Interaction Kinetics for Application to Geochemical Modeling*; U.S. Dept. of the Interior, U.S. Geological Survey: Menlo Park, CA,**2004**.

31. 31.

Marty, N. C.
M.; Claret, F.; Lassin, A.; Tremosa, J.; Blanc, P.; Made, B.; Giffaut, E.; Cochepin, B.;Tournassa t, C. A database of dissolution and precipitation rates for clay-rocks minerals *Appl. Geochem.***2015**, 55, 108– 118 DOI: 10.1016/j.apgeochem.2014.10.012

[Crossref], [CAS]

32. 32.

Cho, Y.; Eker, E.; Uzun, I.; Yin, X.; Kazemi, H. *Rock Characterization in Unconventional Reservoirs: A Comparative Study of Bakken, Eagle Ford, and Niobrara Formations*. In Society of Petroleum Engineers.

33. 33.

Molins, S.; Trebotich, D.; Yang, L.; Ajo-Franklin, J. B.; Ligocki, T. J.; Shen, C.; Steefel, C. I. Pore-Scale Controls on Calcite Dissolution Rates from Flow-through Laboratory and Numerical Experiments *Environ. Sci. Technol.* **2014**, 48 (13) 7453– 7460 DOI: 10.1021/es5013438

[ACS Full Text], [CAS]

34. 34.

Peters, C. A. Accessibilities of reactive minerals in consolidated sedimentary rock: An imaging study of three sandstones *Chem. Geol.* **2009**, 265 (1–2) 198– 208 DOI: 10.1016/j.chemgeo.2008.11.014

[Crossref], [CAS]

35. 35.

Bourg, I. C. Sealing Shales versus Brittle Shales: A Sharp Threshold in the Material Properties and Energy Technology Uses of Fine-Grained Sedimentary Rocks *Environ. Sci. Technol. Lett.* **2015**, 2 (10) 255– 259DOI: 10.1021/acs.estlett.5b00233

[ACS Full Text], [CAS]